https://doi.org/10.1016/j.apcatb.2020.119857

Interface Engineered $NiFe_2O_{4-x}/NiMoO_4$ Nanowire Arrays for Electrochemical Oxygen Evolution

Juhyung Choi,[a,†] Daekyu Kim,[b,†] Weiran Zheng,[b] Bingyi Yan,[a] Yong Li,[b] Lawrence Yoon Suk Lee,[b,c,] Yuanzhe Piao[a,d,]**

[a] Department of Transdisciplinary Studies, Graduate School of Convergence Science and Technology, Seoul National University, 145 Gwanggyo-ro, Yeongtong-gu, Suwon-si, Gyeonggi-do, 16229, Republic of Korea

[b] Department of Applied Biology and Chemical Technology and the State Key Laboratory of Chemical Biology and Drug Discovery, The Hong Kong Polytechnic University, Hung Hom, Kowloon, Hong Kong SAR

[c] Research Institute for Smart Energy, The Hong Kong Polytechnic University, Hung Hom, Kowloon, Hong Kong SAR

[d] Advanced Institutes of Convergence Technology, 145 Gwanggyo-ro, Yeongtong-gu, Suwon-si, Gyeonggi-do, 16229, Republic of Korea

[†] These authors equally contributed to this work.

Corresponding authors

* Lawrence Yoon Suk Lee: Tel.: +852 3400 8696; Fax: +852 2364 9932; E-mail: lawrence.ys.lee@polyu.edu.hk

* Yuanzhe Piao: Tel.: +82 31 888 9141; Fax: +82 31 888 9148; E-mail: parkat9@snu.ac.kr

Abstract

Designing highly active and stable electrocatalysts for oxygen evolution reaction (OER) is the key to success in sustainable water splitting reaction, a sustainable route towards high purity hydrogen production. Interface engineering is one of the most effective strategies for modulating the local electronic structure of active sites to enhance catalytic activity. Herein, $NiFe_2O_{4-x}$ nanoparticles were integrated to $NiMoO_4$ nanowires ($NiFe_2O_{4-x}$/NMO) grown on nickel foam to construct an extended interface with strong electronic interactions. The $NiFe_2O_{4-x}$/NMO demonstrates high OER activities as manifested by a low overpotential of 326 mV at a high current density of 600 mA cm^{-2} and good long-term stability. The intimate interface between $NiFe_2O_{4-x}$ and $NiMoO_4$ is responsible for the Fe-facilitated phase transition to active γ-NiOOH phase as revealed by *in situ* Raman spectroelectrochemical studies. This study outlines how the interface design of integrated nanostructures can optimize the formation of active phase for enhanced catalytic activity.

Keywords: interface engineering; Prussian blue analog; oxygen evolution reaction; electrocatalysis; active surface phase

1. Introduction

Electrochemical water splitting has emerged as a promising technology for producing hydrogen, a clean and renewable energy carrier [1, 2]. The efficiency of overall water electrolysis is kinetically controlled by the more sluggish anodic oxygen evolution reaction (OER) [3, 4]. Noble metal catalysts such as RuO_2 and IrO_2 can significantly reduce the overpotential for OER, but their scarcity and high cost impede their use in the practical application of water splitting [5]. Over the past decade, transition metal-based materials (Fe, Co, and Ni oxides, hydroxides, and oxyhydroxides) have shown high conversion efficiencies towards OER [5, 6]. Furthermore, the composites made of binary or ternary transition metal systems allow the fine tuning of interaction with the substrate, leading to improved reaction efficiency as well as stability [7, 8]. Although such transition metal composites can deliver overpotential values close to those of noble metal-based catalysts, achieving continuous and stable OER performance at high current density ($\geq$ 500 mA cm^{-2}) still remains a challenge [9, 10].

The optimizations for structural and electronic configuration must be considered in order to realize a high current (high reaction rate) at low overpotential. Increasing the surface area of an electrocatalyst can expose more active sites, thus boosting the reaction rate at a given overpotential [11, 12]. Lower contact resistance, which is often needed for high energy efficiency, can be achieved by directly growing nanostructured catalysts on a conductive substrate [13, 14]. Also, the pores in nanostructures are known to be beneficial for charge/mass transfer as well as the dissociation of oxygen bubbles during OER [12, 15]. As an atomic scale tool for constructing desired interfaces between nanostructures, interface engineering has been extensively engaged to modulate the electronic configuration of component materials [16-18]. It can combine the structural merits of each component to enhance the reaction kinetic, and thus

boost the catalytic activity and stability of nanocomposites [19-21]. For example, Jiang *et al*. altered the electronic configuration of spinel $NiCo_2O_4$ interface by using double-exchange interaction of cations to tune the binding energy of OER intermediates [22]. Li *et al*. modulated the electronic configuration of the interface between NiS nanodots and NiTe nanoarrays to *in situ* generate active species that can accelerate the formation of M–OOH (M = metal sites) and thereby enhancing the catalytic OER efficiency [23]. The integration of nanoparticles (NPs) onto a nanowire structure allows the creation and fine tuning of abundant interfaces that are easily accessible for substrates. The increased population of surface active sites together with the facilitated electron transfer in the conductive nanowire arrays can produce highly efficient catalytic system. However, the fabrication of such composites often suffers from the agglomeration and deformation of NPs during electrode preparation as well as electrolysis, eventually compromising the structural stability and performance of composite [24, 25]. A rational synthetic approach is required to construct well-defined and rigid NP/nanowire interfaces to consolidate the structural and collegial advantages while avoiding the stability problem.

Herein, we report a novel nanoarchitecture of oxygen vacancy-rich $NiFe_2O_{4-x}$ NPs anchored on $NiMoO_4$ (NMO) nanowire arrays. NiFe Prussian blue analogs (NiFe PBA) were first immobilized on the NMO nanowires that were grown on a Ni foam by a simple hydrothermal method. The subsequent thermal treatment converts the NiFe PBA to $NiFe_2O_{4-x}$ NPs, forming an intimate interface with the NMO nanowire that exhibits excellent OER activity with a low overpotential of 326 mV at a high current density of 600 mA cm^{-2} in 1.0 M KOH, as well as good stability (1 % loss in 40 h reaction). The effects of solvent on the growth of NiFe PBA and the resultant $NiFe_2O_{4-x}$ NPs are explored to modulate the interface formation with NMO

nanowire. Based on *in situ* Raman spectroelectrochemical measurements, the phase transition process of $NiFe_2O_{4-x}$/NMO that leads to the formation of active species is studied to understand its excellent OER performance.

2. Experimental Section

2.1. Synthesis of NMO-H on nickel foam

$Ni(NO_3)_2 \cdot 6H_2O$ (0.175 g) and $Na_2MoO_4 \cdot 2H_2O$ (0.145 g) were dissolved in deionized water (DI water, 10 mL) and mixed under stirring for 30 min. This mixed solution was then transferred to a 15 mL Teflon-lined autoclave. A Ni foam (1.0 × 3.5 cm^2) was rinsed with 1.0 M HCl, acetone, and ethanol under sonication for 15 min, respectively. This pre-treated Ni foam was then put into the autoclave containing the mixed solution, followed by heating at 150 ℃ for 4 h. After natural cooling to 25 ℃, the sample was taken out, rinsed with DI water and ethanol, and dried in the vacuum oven at 60 ℃ for 12 h.

2.2. Synthesis of NiFe PBA/NMO-H composites

Briefly, 0.8 mg of $K_3[Fe(CN)_6]$ was dissolved in a 10 mL mixed solution of ethanol and H_2O [three-volume ratios (EtOH : H_2O = 25:75, 75:25, and 100:0)]. The as-prepared NMO-H on Ni foam were placed in these solutions and kept for 3 h under stirring, respectively. The samples were taken out, rinsed using ethanol, and dried in a vacuum oven at 60 ℃ for 12 h. The obtained samples were denoted as NiFe PBA/NMO-H-25, NiFe PBA/NMO-H-75, and NiFe PBA/NMO-H-100 based on the percentage of EtOH used.

2.3. Preparation of $NiFe_2O_{4-x}$/NMO composites

The as-obtained NiFe PBA/NMO-H composites on Ni foam were calcined at 400 ℃ for 2 h (heating rate = 3 ℃ min^{-1}) under air flow. For comparison, the NMO-H on the Ni foam was also calcined under the same conditions. The mass loading of the as-prepared samples is shown in Table S1.

2.4. Materials characterizations

The surface morphology of materials was studied by a field emission-scanning electron microscope (FE-SEM, Hitachi S-4800). Further characterization of morphology and structure was performed using a high-resolution transmission electron microscope (HRTEM, JEOL JEM-2010F). Raman spectra were acquired using a 785 nm excitation laser on a Raman spectrometer (Confocal Micro Raman Spectroscopy System, Renishaw). The crystal structures of materials were investigated by X-ray diffractometer (XRD, Bruker D8-Advance, Cu Kα radiation). Fourier-transform infrared (FTIR, Nicolet 6700 spectrometer) spectra were obtained in the range of 400 to 4000 cm^{-1}. X-ray photoelectron spectroscopy (XPS) was carried out on an AXIS-His spectrometer. The Al K_α was used as an X-ray source. A Casa XPS software was employed to analyze the acquired XPS spectra. A BELSORP-mini II instrument was used to obtain nitrogen adsorption-desorption isotherms. The oxygen vacancy of samples was characterized by an Electron paramagnetic resonance (EPR) spectrometer (ADANI SPINSCAN X spectrometer). For a precise comparison of EPR spectra, the same mass loading was used for all the samples. Thermal analysis was carried out on a TGA/DSC1 (Mettler Toledo Corporation instrument) from 25 to 700 ℃ with a heating rate of 3 ℃ min^{-1} in airflow.

2.5. *In situ* Raman spectroelectrochemical investigation

A Raman spectrometer (Confocal Micro-Raman Spectroscopy System, Renishaw) equipped with a 50x objective lens was used with a customized electrochemical cell for *in situ* Raman

measurement. The 785 nm stream-line excitation laser with a power of 1.5 mW was used to obtain Raman spectra. The prepared catalysts, Pt wire, and Hg/HgO electrode (1.0 M KOH) were served as the working, counter, and reference electrodes, respectively. The *in situ* Raman spectrum of each working electrode was recorded three times from 100 to 1200 cm^{-1} with an acquisition time of 20 s at different potentials during a current-time (*i*-t) measurement. The applied potential was increased stepwise from 0.93 to 1.63 V with an interval of 0.05 V. At each step, the potential was applied for three minutes. After the initial activation steps, the samples were further activated by 35 cycles of cyclic voltammetric (CV) scans, and another set of *in situ* Raman spectra was collected in the applied potential range from 0.93 to 1.73 V.

2.6. Electrochemical measurements

All the electrochemical tests were conducted on an electrochemical workstation (Metrohm AG Autolab workstation, PGSTAT 302N) with a standard three-electrode system in O_2-saturated 1.0 M KOH. The prepared catalysts (0.5 × 1.0 cm^2) were served as the working electrode. For the counter and reference electrodes, the Pt plate and the Hg/HgO electrode (1.0 M KOH) were used, respectively. All potentials in this manuscript were calibrated to a reversible hydrogen electrode (RHE) value according to the Eq. (1): $E_{RHE} = E_{Hg/HgO} + 0.14 + 0.059 \times pH$. Linear sweep voltammetry (LSV) was performed at a scan rate of 0.5 mV s^{-1} to avoid the interference from Ni oxidation current. Prior to LSV measurements, the samples activated by 35 CV cycles between 1.0 and 1.8 V at a scanning rate of 5 mV s^{-1}. Electrochemical impedance spectra (EIS) were recorded in a frequency range of 0.1 Hz-100 kHz with a 5 mV amplitude at 1.52 V. Double-layer capacitance (C_{dl}) was estimated based on the CV curves recorded in the non-faradaic region (1.00 to 1.10 V) at various scan rates. Linear slope was extracted from the plot of capacitive current densities (ΔJ, $J_{anodic} - J_{cathodic}$) at 1.05 V as a function of scan rates, where the C_{dl} was

estimated as half of the linear slope. Chronoamperometry was performed for 40 h at the fixed potentials to evaluate the stability of the catalysts. All polarization curves in this manuscript were corrected with a 65 % *i*R compensation unless otherwise stated.

3. Results and discussion

3.1. Preparation and characterization of NiFe PBA/NMO-H arrays

The schematics shown in **Fig. 1a** illustrates the procedure for fabricating $NiFe_2O_{4-x}$ NPs-integrated NMO nanowires on Ni foam. First, hydrated NMO nanowires ($NiMoO_4 \cdot H_2O$, NMO-H) were vertically grown on a Ni foam by a hydrothermal synthesis [26]. NiFe PBA was then formed on the NMO-H by *in situ* ion exchange reaction (NiFe PBA/NMO-H) [27], in which the size of NiFe PBA was tuned by varying the solvent composition (water/ethanol mixture) and thus solvent polarity. The NiFe PBA/NMO-H products were denoted as NiFe PBA/NMO-H-25, NiFe PBA/NMO-H-75, and NiFe PBA/NMO-H-100 based on the vol.% of water used in the ion exchange reaction. The subsequent thermal decomposition of NiFe PBA/NMO-H yielded the $NiFe_2O_{4-x}$ NPs-integrated NMO nanowires ($NiFe_2O_{4-x}$/NMO).

Scanning electron microscopy (SEM) images in **Fig. S1a** and **S1b** show the uniform distribution of NMO-H nanowires (average length = 3.5 μm) on the Ni foam. Similar nanowire structures are observed from the NiFe PBA/NMO-H-25 with the surface of NMO-H covered with tiny NiFe PBA NPs (**Fig. S1c** and **S1d**). Transmission electron microscopy (TEM) image of the NiFe PBA/NMO-H-25 reveals the tightly packed NiFe PBA NPs (average d = 16 nm) that appear almost as a film on NMO-H nanowire (**Fig. S2a**). Energy dispersive X-ray (EDX) elemental mapping confirms that Mo and O atoms are mainly located in the core of the NMO-H nanowire, while Fe and K atoms are mostly found on the NiFe PBA NPs (**Fig. S2c**). This is well explained by the surface dissolution of MoO_4^{2-} for ion exchange with K^+ and $[Fe(CN)_6]^{3-}$ [28],

leading to the formation of NiFe PBA NPs. Fourier-transform infrared (FT-IR) spectrum of NiFe PBA/NMO-H-25 identifies the characteristic peak for cyanide group (–CN) at *ca*. 2100 cm^{-1}, which corresponds to the stretching vibrations in Fe^{III}–CN–Ni^{II} in the PBA structure (**Fig. S3a** and **S3b**) [27]. The X-ray diffraction (XRD) pattern of NMO-H matches that of the hydrated $NiMoO_4$ (JCPDS 13-0128) [29], while NiFe PBA/NMO-H-25 shows two additional peaks at 17.3° and 24.6°, which are ascribed to the (200) and (220) planes of $KNi[Fe(CN)_6]$, respectively (JCPDS 51-1897, **Fig. S3c**), confirming the formation of NiFe PBA [30]. Interestingly, the size of NiFe PBA NPs increases from 16 to 84 and 128 nm as the volume ratio of water in the reaction solution changes from 25 to 75 and 100%, respectively (**Fig. S4**). The low solubility of $K_3[Fe(CN_6)]$ in ethanol is believed to affect the nucleation and growth rates of NiFe PBA [31].

3.2. Preparation and characterization of $NiFe_2O_{4-x}$/NMO arrays

The calcination of NiFe PBA/NMO-H-25 at 400 ℃ under air atmosphere converted NiFe PBA to $NiFe_2O_{4-x}$ NPs on the NMO surface, maintaining the core/shell-type nanowire structure. The –CN group connecting Ni and Fe atoms in PBA is thermally decomposed, releasing CO_2 and NO_x gases that may create pores as they escape [32, 33]. For comparison, NMO-H nanowires were also calcined under the same conditions and denoted as NMO. The morphology and structure of $NiFe_2O_{4-x}$/NMO and NMO were first investigated by SEM. The as-prepared $NiFe_2O_{4-x}$/NMO-25 exhibits a NPs-integrated nanowire morphology similar to that of NiFe PBA/NMO-H (**Fig. 1b** and **1c**). The average diameter of NPs on $NiFe_2O_{4-x}$/NMO-25 has decreased to 11 nm compared with those on NiFe PBA/NMO-H-25 (16 nm) due to thermal decomposition. The XRD patterns of $NiFe_2O_{4-x}$/NMO-25 and NMO (**Fig. 1d**) are similar and both can be assigned to $NiMoO_4 \cdot H_2O$ (JCPSD 13-0128). An additional peak at 18.6° is observed from $NiFe_2O_{4-x}$/NMO-25 and assigned to the (111) plane of spinel $NiFe_2O_4$ (JCPDS 74-1913). This peak is weak and broad

due to the relatively small amount of $NiFe_2O_{4-x}$ compared with NMO, as well as the low crystallinity of $NiFe_2O_{4-x}$. Thermogravimetric analysis (TGA) confirms the removal of both chemically and physically absorbed hydrates of NMO-H without phase transformation during the calcination process at 400 °C (**Fig. S6**). Raman spectroscopy was engaged to further characterize the structures of $NiFe_2O_{4-x}$/NMO-25 and NMO (**Fig. 1e**). Both $NiFe_2O_{4-x}$/NMO-25 and NMO display characteristic Raman peaks at 354, 828, 871, and 948 cm^{-1}, which are attributed to the Mo-O vibration modes of $NiMoO_4$, a result that is in good agreement with previous reports [29, 34]. In addition, the broad Raman band at *ca*. 550 cm^{-1} of $NiFe_2O_{4-x}$/NMO-25, echoing results of the XRD analysis, suggests a structural disorder of Ni–Fe oxide [35].

Fig. 2 compares the TEM and EDX elemental mapping images of $NiFe_2O_{4-x}$/NMO samples. The TEM image of $NiFe_2O_{4-x}$/NMO-25 (**Fig. 2a**) clearly shows the integration of $NiFe_2O_{4-x}$ NPs on the NMO nanowire. These $NiFe_2O_{4-x}$ NPs exhibit a narrow size distribution (average d = 11 nm), which is smaller than their precursor, NiFe PBA NPs (*ca*. 16 nm), due to the loss of –CN ligands by thermal decomposition (**Fig. S7a**). The HRTEM image in **Fig. 2b** reveals three distinct domains (areas I, II, and III) of $NiFe_2O_{4-x}$/NMO-25: low-crystalline $NiFe_2O_{4-x}$ (area I), polycrystalline NMO (area III), and the interface of $NiFe_2O_{4-x}$ and NMO (area II) as further proved by the corresponding fast Fourier transform (FFT) diffraction patterns. The lattice spacing of 1.89 Å observed from $NiFe_2O_{4-x}$ can be assigned to the (331) plane of $NiFe_2O_4$ (**Fig. 2c**). Elemental mapping images (**Fig. 2d**) indicate that Fe and Mo atoms are particularly concentrated on the outer and inner structures, respectively, while Ni atoms are uniformly distributed over the entire area, confirming the $NiFe_2O_{4-x}$/NMO-25 structure.

Changes in solvent polarity during NiFe PBA formation affect the size of PBA NPs as well as that of the resultant $NiFe_2O_{4-x}$ NPs. **Fig. 2e** and **2i** are the TEM images of $NiFe_2O_{4-x}$/NMO-75

and $NiFe_2O_{4-x}$/NMO-100 that show the integrated $NiFe_2O_{4-x}$ NPs of *ca*. 51 and 70 nm, respectively (**Fig. S7b** and **S7c**). Similar to $NiFe_2O_{4-x}$/NMO-25, both $NiFe_2O_{4-x}$/NMO-75 and $NiFe_2O_{4-x}$/NMO-100 display a weak XRD peak at 18.6° in addition to the features of NMO, indicating the (111) plane of spinel $NiFe_2O_4$ (**Fig. S8**). The HRTEM images shown in **Fig. 2g** and **2k** reveal the lattice fringes of $NiFe_2O_{4-x}$/NMO-75 and $NiFe_2O_{4-x}$/NMO-100, which exhibit the *d*-spacing of 2.49 and 1.59 Å matching the (331) and the (511) planes of $NiFe_2O_4$, respectively. The presence of three domains of areas I, II, and III are also evident as supported by the corresponding FFT patterns (**Fig. 2f** and **2j**). Moreover, the elemental distributions of $NiFe_2O_{4-x}$/NMO-75 and $NiFe_2O_{4-x}$/NMO-100 (**Fig. 2h** and **2l**) clearly show the interfacial boundaries between $NiFe_2O_{4-x}$ and NMO. It is worth noting that although the contact interface between $NiFe_2O_{4-x}$ NPs and NMO nanowire increases with the size of $NiFe_2O_{4-x}$ NPs, the $NiFe_2O_{4-x}$ film covering the NMO nanowire diminishes.

The CO_2 and NO_x gases released during the thermal decomposition of NiFe PBA may induce pores in $NiFe_2O_{4-x}$. Nitrogen adsorption-desorption isotherm was obtained to determine the surface area and total pore volume of $NiFe_2O_{4-x}$/NMO samples (**Fig. 3a**). Brunauer–Emmett–Teller (BET) surface area analyses indicate the mesoporous feature of all samples with a specific area of 50.6, 52.6, and 67.1 $m^2\ g^{-1}$ for $NiFe_2O_{4-x}$/NMO-100, $NiFe_2O_{4-x}$/NMO-75, and $NiFe_2O_{4-x}$/NMO-25, respectively (**Table S2**). In addition, the increasing number of pores under 5 nm implies the formation of pores inside the $NiFe_2O_{4-x}$/NMO-25 sample (inset in **Fig. 3a**).

To further elucidate the surface electronic configuration and chemical composition, X-ray photoelectron spectroscopy (XPS) was conducted on the $NiFe_2O_{4-x}$/NMO nanostructures. The survey spectra confirm the coexistence of Ni, Fe, Mo, and O elements in all samples (**Fig. S9a**). The surface Ni/Fe atomic ratio for $NiFe_2O_{4-x}$/NMO-25 is 2.4 and this ratio increases in

$NiFe_2O_{4-x}$/NMO-75 (3.3) and $NiFe_2O_{4-x}$/NMO-100 (6.3), suggesting that $NiFe_2O_{4-x}$ NPs are better distributed on the NMO surface in the $NiFe_2O_{4-x}$/NMO-25 due to their smaller size (**Table S3**). High-resolution Ni 2p spectra of all samples can be deconvoluted to the two pairs of spin-orbit peaks (Ni $2p_{3/2}$ and Ni $2p_{1/2}$) accompanying broad satellites (**Fig. 3b**, left). The fitted Ni $2p_{3/2}$ and Ni $2p_{1/2}$ peaks at 855.6 and 873.2 eV, respectively, are assigned to Ni^{2+} species, while those at higher binding energies (858.1 and 875.7 eV) are attributed to Ni^{3+} species [36]. These peaks exhibit slight positive shifts of 0.15 eV compared with those observed from the NMO spectrum (**Fig. S10a**). A similar positive shift of Mo 3d peak is evident when $NiFe_2O_{4-x}$ NPs are integrated on NMO (**Fig. S10b**), which implies strong electronic interaction between $NiFe_2O_{4-x}$ and NMO [37]. The presence of Ni^{3+} species strongly suggests the presence of oxygen vacant sites in the $NiFe_2O_{4-x}$ [38, 39]. The ratio of Ni $2p_{3/2}$ Ni^{3+} to Ni^{2+} peak intensities, as estimated by peak area, decreases from 0.61 in $NiFe_2O_{4-x}$/NMO-25 to 0.48 in $NiFe_2O_{4-x}$/NMO-75 and 0.25 in $NiFe_2O_{4-x}$/NMO-100, indicating the $NiFe_2O_{4-x}$ NPs in $NiFe_2O_{4-x}$/NMO-25 possesses more oxygen defects. It is believed that the smaller size of $NiFe_2O_{4-x}$ NP can enable more efficient re-distribution of valence states and stronger electronic interaction with NMO because the active sites on NP are located closer to the interface [22, 40].

The O 1s spectra acquired from $NiFe_2O_{4-x}$/NMO samples (**Fig. 3b**, right) exhibit three characteristic peaks corresponding to the lattice oxygen in $NiFe_2O_4$ (O1; 530.3 eV), lattice oxygen in $NiMoO_4$ (O2; 530.8 eV), and surface-adsorbed oxygen (O3; 533.1 eV) [41-43]. Another peak at 531.6 eV could be attributed to the surface oxygen defects/vacancy species [44]; its relative peak area is small in $NiFe_2O_{4-x}$/NMO-100, but it increases to 3.3 in $NiFe_2O_{4-x}$/NMO-75 and 8.1 in $NiFe_2O_{4-x}$/NMO-25. The oxygen defects in the $NiFe_2O_{4-x}$/NMO composites were also probed using electron paramagnetic resonance (EPR) spectroscopy (**Fig. S11**). All three

$NiFe_2O_{4-x}$/NMO samples show symmetric EPR signals at g = 2.00 that can be attributed to the characteristic trapped electron at oxygen vacancies [44, 45]. Comparison of the EPR signal intensities confirms that $NiFe_2O_{4-x}$/NMO-25 contains the highest oxygen vacancy concentration, a result that is in good agreements with XPS analyses.

3.3. Electrochemical properties

3.3.1. Oxygen evolution reaction (OER) performance

The electrocatalytic OER performances of all prepared samples were tested in a three electrode-cell in alkaline media (1.0 M KOH). **Fig. 4a** presents the linear sweep voltammograms (LSV, *i*R corrected) of the as-prepared samples. The peak observed in the potential range of 1.38 to 1.43 V (*vs*. RHE) is related to the oxidation of Ni species to a higher valence state [46]. The polarization curve of $NiFe_2O_{4-x}$/NMO-25 reveals the lowest overpotential (η) of 262 mV at a current density of 10 mA cm^{-2} compared with those of $NiFe_2O_{4-x}$/NMO-75 (273 mV), $NiFe_2O_{4-x}$/NMO-100 (292 mV), NiFe PBA/NMO-H-25 (304 mV), and NMO (309 mV). The Ni foam shows almost no contribution to the catalytic activity at similar overpotential values. Also, the $NiFe_2O_{4-x}$/NMO-25 delivers a high current density of 600 mA cm^{-2} at an overpotential of 326 mV. The corresponding Tafel plots (η *vs.* log (*j*)) are shown in **Fig. 4b**, where a diminishing trend of Tafel slope is observed from $NiFe_2O_{4-x}$/NMO-100 (60.9 mV dec^{-1}) to $NiFe_2O_{4-x}$/NMO-75 (52.11 mV dec^{-1}) and $NiFe_2O_{4-x}$/NMO-25 (41.9 mV dec^{-1}). Meanwhile, NMO exhibits the largest Tafel slope of 101.7 mV dec^{-1}. The Tafel slope can be used to reveal the rate-determining step that is crucial for understanding the reaction mechanism [47]. Based on the Tafel slopes, $NiFe_2O_{4-x}$/NMO-100 and NMO go through the same rate-determining step (the second step, M–OH* $\rightarrow$ M–O* + H^+ + e^-), however, a large difference in their Tafel slopes (*ca*. 40 mV dec^{-1}) suggests a distinct reaction kinetics. Much smaller Tafel slopes of $NiFe_2O_{4-x}$/NMO-25 and

$NiFe_2O_{4-x}$/NMO-75 indicate that the O–O bond formation ($M–O^* + OH^- \rightarrow M–OOH^* + e^-$) is the rate-determining step due to decreased reaction barrier. This can be attributed to the low-spin Ni^{3+} valence state at the vicinity of interface, which favors the chemisorption of oxygen-containing intermediates [23, 37]. **Fig. 4c** compares the electrocatalytic performances of the as-prepared $NiFe_2O_{4-x}$/NMO-25 with the recently reported Ni- or Fe-based catalysts, and the remarkable performance of $NiFe_2O_{4-x}$/NMO-25 is clearly demonstrated (data shown in **Table S4**). The superior performance of $NiFe_2O_{4-x}$/NMO-25 compared with the other $NiFe_2O_{4-x}$/NMO samples can be reasoned with the enhanced electrochemical surface area due to its smallest $NiFe_2O_{4-x}$ NP (11 nm). This is supported by the double-layer capacitance (C_{dl}) measurements (**Fig. 4d**). The C_{dl} of $NiFe_2O_{4-x}$/NMO-25 reaches the highest value of 2.13 mF cm^{-2}, which is nearly 1.7 and 2.8 times of those of $NiFe_2O_{4-x}$/NMO-75 (1.25 mF cm^{-2}) and $NiFe_2O_{4-x}$/NMO-100 (0.75 mF cm^{-2}), respectively. For comparison, the C_{dl} of the NMO and NiFe PBA/NMO-H-25 are merely 0.57 and 0.4 mF cm^{-2}, respectively.

3.3.2. Charge-transfer kinetics

Electrochemical impedance spectroscopy (EIS) was also engaged to gain further insights into the high OER activity of $NiFe_2O_{4-x}$/NMO-25. The Nyquist plots presented in **Fig. 4e** show that the $NiFe_2O_{4-x}$/NMO composites possess much lower charge transfer resistance (R_{ct}) values than NMO (3.421 Ω) and NiFe PBA/NMO-H-25 (3.777 Ω, data summarized in **Table S5**). Among the $NiFe_2O_{4-x}$/NMO catalysts, $NiFe_2O_{4-x}$/NMO-25 has the lowest R_{ct} of 0.362 Ω, which implies a faster charge-transfer to the $NiFe_2O_{4-x}$ NPs [48]. The size of $NiFe_2O_{4-x}$ NPs is believed to be an important factor that determines the OER activity for several reasons. The smaller $NiFe_2O_{4-x}$ NP can provide the larger electrochemical active surface area with less charge transfer resistance, and the entire $NiFe_2O_{4-x}$ NP is close to the interface with NMO which would intensify the local

electronic interaction. Moreover, the higher concentration of oxygen vacant sites in $NiFe_2O_{4-x}$/NMO-25 is expected to contribute to the enhanced catalytic performance by lowering the adsorption energy of water [49].

3.3.3. Stability test

Long-term operational stability is another essential criterion for the practical application of the electrocatalyst, which was tested by conducting chronoamperometry at 1.55 and 1.65 V (**Fig. 4f**). The $NiFe_2O_{4-x}$/NMO-25 electrode demonstrates excellent durability at a high current density of 200 mA cm^{-2}, showing only *ca*. 1 % loss during the continuous 40-hour reaction. The structural stability of $NiFe_2O_{4-x}$/NMO-25 can also be confirmed by the unchanged LSV curve (inset in **Fig. 4f**) as well as its nanowire morphology (**Fig. S13**) after a continuous 40-hour reaction. Such high structural stability could be attributed to the strong interfacial interaction between $NiFe_2O_{4-x}$ and NMO.

3.4. *In situ* Raman spectroelectrochemical study

Phase transformation of electrocatalysts, which widely occurs in many catalytic reactions, is a key step for establishing the required overpotential, in particular, for multi-electron transfer reactions such as OER. In order to investigate the phase transition during electrocatalysis, we employed *in situ* Raman spectroelectrochemistry. The freshly prepared $NiFe_2O_{4-x}$/NMO-25 electrode was first analyzed for its activation at different potentials in 1.0 M KOH. The Raman spectrum acquired at 0.93 V *vs*. RHE exhibits similar Mo–O vibrations as previously observed in **Fig. 1e** with slight red-shifts (**Fig. S14**), which are caused by the dissolution of molybdenum oxide in alkaline solution [50]. As the applied potential increases from 0.93 to 1.28 V, a broad peak develops at *ca*. 526 cm^{-1}, which is attributed to the formation of a FeOOH intermediate (**Fig. 5a** and **5b**). At 1.33 V, a new peak appears at 495 cm^{-1} and is assigned to the disordered

Ni–OH that could be transformed into NiOOH phase at higher potentials [51]. It is suggested that Fe sites are more favorable for adsorbing OH^- than Ni sites at lower potentials, while the Fe^{3+} species induces the formation of high valence Ni species that preferably binds to OH^- at higher potentials [7]. When the anodic potential reaches 1.38 V, two other peaks evolve at 477 and 558 cm^{-1} and intensify at higher potentials. These two peaks correspond to the Ni–O bending and stretching vibrations of γ-NiOOH phase, respectively. With the average valance state of $Ni^{3.6+}$, γ-NiOOH phase was reported to accelerate OER in alkaline electrolytes [52]. The Raman bands of γ-NiOOH phase become more obvious at an applied potential of 1.43 V. Meanwhile, the Raman signals for Mo–O vibrations gradually decrease in the potential range from 1.28 to 1.48 V as a result of Mo–O conversion to MoO_4^{2-}, and disappear at 1.53 V (**Fig. 5c**).

To further understand the role of $NiFe_2O_{4-x}$ NPs, these results were compared with the *in situ* Raman spectra of NMO electrode (**Fig. S15a**). The two Raman peaks of γ-NiOOH phase start to appear at 1.43 V, replacing the weak Raman features of Ni–OH, and intensifying at higher potentials, indicating that the active phase transformation of NMO electrode requires 0.05 V higher potential compared with $NiFe_2O_{4-x}$/NMO-25. This is consistent with the difference in the pre-oxidation peak potentials observed in the LSV curves (**Fig. 4a**). On the other hand, the Mo–O vibrations in NMO electrode completely vanish at 1.48 V, which happens at 1.53 V in the case of $NiFe_2O_{4-x}$/NMO-25. The Fe sites in $NiFe_2O_{4-x}$ are believed to alleviate the Mo leaching from NMO at a lower potential range [35]. It should be noted that the γ-NiOOH band in the $NiFe_2O_{4-x}$/NMO-25 spectra is slightly reduced at 1.58 V, whereas that of NMO still remains intense at up to 1.68 V. Such Raman peak decrease in $NiFe_2O_{4-x}$/NMO-25 is caused by the formation of bubbles on the catalyst surface, confirming the oxygen evolution [53]. This

observation indicates that OER takes place at a lower potential in $NiFe_2O_{4-x}$/NMO-25 than NMO during the activation step.

After the initial activation step, the *in situ* Raman spectra of $NiFe_2O_{4-x}$/NMO-25 and NMO electrodes were recorded again to observe the structural evolution and compare the OER properties (**Fig. S16**). At 0.93 V, both electrodes display strong γ-NiOOH bands at 477 and 558 cm^{-1}, suggesting the complete activation of the electrode surface. From the spectrum of the NMO electrode, however, the $Ni(OH)_2$ peak is also observed, indicating the incomplete $Ni(OH)_2$–NiOOH transformation during the activation process. In contrast, the Raman spectra of $NiFe_2O_{4-x}$/NMO-25 shows only the γ-NiOOH bands with no additional peaks related to the Fe and Mo species. The γ-NiOOH bands of $NiFe_2O_{4-x}$/NMO-25 diminish when the applied potential reaches 1.53 V, while those of NMO still remain until 1.73 V. This explains the high OER activity of $NiFe_2O_{4-x}$/NMO-25 promoted by the active γ-NiOOH phase at a lower potential, thanks to the Fe-facilitated surface reconstruction [51, 54]. The post-OER TEM image clearly shows the altered surface morphology of $NiFe_2O_{4-x}$/NMO-25 (**Fig. 6a**). A thin γ-NiOOH layer (*ca*. 5 nm) is evident on the edge, providing additional evidence of phase transition, while ultrasmall NPs (average d = 1.3 nm), which are believed to be $NiFe_2O_{4-x}$ NPs of reduced size, are observed from the inner core (**inset in Fig. 6a**). This is supported by the even distribution of Fe atoms in the corresponding EDX elemental mapping (**Fig. 6b**). It is also noted that almost no Mo atoms are detected, indicating that Mo atoms are mostly dissolved away from the $NiFe_2O_{4-x}$/NMO-25 during OER, which agrees well with the *in situ* Raman measurements. Furthermore, the XPS investigation after OER reveals that the ratio of Ni^{3+} to Ni^{2+} peak intensities of $NiFe_2O_{4-x}$/NMO-25 has increased to 2.1 compared with the 0.61 of fresh $NiFe_2O_{4-x}$/NMO-25 (**Fig. 6c**), confirming the formation of γ-NiOOH phase. Also, the O 1s

spectrum displays two major peaks of similar intensities at 530.5 and 531.2 eV assigned to the lattice oxygen and hydroxide as well as a largely enhanced peak for surface-adsorbed H_2O, supporting the formation of NiOOH (**Fig. 6d**) [14, 55].

4. Conclusion

In summary, we fabricated an integrated $NiFe_2O_{4-x}$/NMO electrocatalyst *via* interfacial engineering to achieve high OER performance. By tuning the solvent polarity, the growth of NiFe PBA precursor was controlled, which enabled the construction of $NiFe_2O_{4-x}$/NMO heterogeneous structure with extended solid-solid interface, resulting in strong electronic interaction between $NiFe_2O_{4-x}$ NPs and NMO nanowires. The $NiFe_2O_{4-x}$/NMO electrocatalyst exhibited superior OER activity with an overpotential of 326 mV at a high current density of 600 mA cm^{-2}, as well as good long-term stability for 40 h at 200 mA cm^{-2}. *In situ* Raman spectroelectrochemical studies revealed the potential-dependent phase transition of the $NiFe_2O_{4-x}$/NMO-25 and fast surface reconstruction during the OER process. The Fe sites in $NiFe_2O_{4-x}$ NPs act as strong Lewis acid to induce and stabilize the higher valence Ni species for efficient phase transformation. This work demonstrates a rational design strategy for achieving active phase to realize cost-effective, highly active, and stable OER catalysis at the nanoscale interface.

Acknowledgements

J. C. and D. K. contributed equally to this work. This work was supported by the Center for Integrated Smart Sensors funded by the Ministry of Science, ICT and Future Planning, Republic of Korea, as Global Frontier Project (CISS-2012M3A6A6054186), Basic Science Research

Program through National Research Foundation of Korea (NRF-2018R1D1A1B07051249), Nano Materials Technology Development Program (NRF-2015M3A7B6027970) funded by the Ministry of Education. The financial supports from the Innovation and Technology Commission of Hong Kong and Hong Kong Polytechnic University (1-BE0Y) are also acknowledged.

References

[1] Y. Jiao, Y. Zheng, M. Jaroniec, S.Z. Qiao, Design of electrocatalysts for oxygen- and hydrogen-involving energy conversion reactions, Chem. Soc. Rev. 44 (2015) 2060-2086.

[2] Z. Seh, J. Kibsgaard, C. Dickens, I. Chorkendorff, J. Norskov, T. Jaramillo, Combining theory and experiment in electrocatalysis: insights into materials design, Science 355 (2017) 146.

[3] N.-T. Suen, S.-F. Hung, Q. Quan, N. Zhang, Y.-J. Xu, H.M. Chen, Electrocatalysis for the oxygen evolution reaction: recent development and future perspectives, Chem. Soc. Rev. 46 (2017) 337-365.

[4] J.S. Kim, B. Kim, H. Kim, K. Kang, Recent progress on multimetal oxide catalysts for the oxygen evolution reaction, Adv. Energy Mater. 8 (2018) 1702774.

[5] C.C.L. McCrory, S. Jung, J.C. Peters, T.F. Jaramillo, Benchmarking heterogeneous electrocatalysts for the oxygen evolution reaction, J. Am. Chem. Soc. 135 (2013) 16977-16987.

[6] I. Roger, M.A. Shipman, M.D. Symes, Earth-abundant catalysts for electrochemical and photoelectrochemical water splitting, Nat. Rev. Chem. 1 (2017) 3.

[7] Z. Qiu, C.-W. Tai, G.A. Niklasson, T. Edvinsson, Direct observation of active catalyst surface phases and the effect of dynamic self-optimization in NiFe-layered double hydroxides for alkaline water splitting, Energy Environ. Sci. 12 (2019) 572-581.

[8] S. Hao, L. Chen, C. Yu, B. Yang, Z. Li, Y. Hou, L. Lei, X. Zhang, NiCoMo hydroxide nanosheet arrays synthesized via chloride corrosion for overall water splitting, ACS Energy Lett. 4 (2019) 952-959.

[9] H. Zhou, F. Yu, J. Sun, R. He, S. Chen, C.-W. Chu, Z. Ren, Highly active catalyst derived from a 3D foam of $Fe(PO_3)_2/Ni_2P$ for extremely efficient water oxidation, Proc. Natl. Acad. Sci. USA. 114 (2017) 5607-5611.

[10] R. Chen, S.F. Hung, D. Zhou, J. Gao, C. Yang, H. Tao, H.B. Yang, L. Zhang, L. Zhang, Q. Xiong, H.M. Chen, B. Liu, Layered structure causes bulk NiFe layered double hydroxide unstable in alkaline oxygen evolution reaction, Adv. Mater. 31 (2019) 1903909.

[11] C. Tang, H.S. Wang, H.F. Wang, Q. Zhang, G.L. Tian, J.Q. Nie, F. Wei, Spatially confined hybridization of nanometer-sized NiFe hydroxides into nitrogen-doped graphene frameworks leading to superior oxygen evolution reactivity, Adv. Mater. 27 (2015) 4516.

[12] H. Xu, H Shang, C. Wang, L. Jin, C. Chen, C. Wang, Y. Du, Three-dimensional open $CoMoO_x/CoMoS_x/CoS_x$ nanobox electrocatalysts for efficient oxygen evolution reaction, Appl. Catal. B: Environ, 265 (2020) 118605.

[13] L. Yu, H. Zhou, J. Sun, F. Qin, F. Yu, J. Bao, Y. Yu, S. Chen, Z. Ren, Cu nanowires shelled with NiFe layered double hydroxide nanosheets as bifunctional electrocatalysts for overall water splitting, Energy Environ. Sci. 10 (2017) 1820-1827.

[14] C. Liang, P. Zou, A. Nairan, Y. Zhang, J. Liu, K. Liu, S. Hu, F. Kang, H.J. Fan, C. Yang, Exceptional performance of hierarchical Ni-Fe oxyhydroxide@NiFe alloy nanowire array electrocatalysts for large current density water splitting, Energy Environ. Sci. 13 (2020) 86-95.

[15] G. Liu, M. Wang, Y. Wu, N. Li, F. Zhao, Q. Zhao, J. Li, 3D porous network heterostructure NiCe@NiFe electrocatalyst for efficient oxygen evolution reaction at large current densities, Appl. Catal. B: Environ. 260 (2020) 118199.

[16] W. Ma, H. Li, S. Jiang, G. Han, J. Gao, X. Yu, H. Lian, W. Tu, Y. Han, R. Ma, Facile, synthesis of superstructured MoS_2 and graphitic nanocarbon hybrid for efficient hydrogen evolution reaction, ACS Sustainable Chem. Eng. 6 (2018) 14441-14449

[17] Y. Jia, L. Zhang, G. Gao, H. Chen, B. Wang, J. Zhou, M. T. Soo, M. Hong, X. Yan, G. Qian, J. Zou, A. Du, X. Yao, A heterostructure coupling of exfoliated Ni–Fe hydroxide nanosheet and defective graphene as a bifunctional electrocatalyst for overall water splitting, Adv. Mater. 29 (2017) 1700017

[18] Y. Zhou, Z. Wang, Z. Pan, L. Liu, J. Xi, X. Luo, Y. Shen, Exceptional performance of hierarchical Ni–Fe (hydr)oxide@NiCu electrocatalysts for water splitting, Adv. Mater. 31 (2019) 1806769

[19] X. Luo, P. Ji, P. Wang, R. Cheng, D. Chen, C. Lin, J. Zhang, J. He, Z. Shi, N. Li, S. Xiao, S. Mu, Interface engineering of hierarchical branched Mo-doped Ni_3S_2/Ni_xP_y hollow

heterostructure nanorods for efficient overall water splitting, Adv. Energy Mater. 10 (2020) 1903891.

[20] D. Kim, J. Resasco, Y. Yu, A.M. Asiri, P. Yang, Synergistic geometric and electronic effects for electrochemical reduction of carbon dioxide using gold–copper bimetallic nanoparticles, Nat. Commun. 5 (2014) 4948.

[21] T. Zhou, N. Zhang, C. Wu, Y. Xie, Surface/interface nanoengineering for rechargeable Zn-air batteries, Energy Environ. Sci. 13 (2020) 1132-1153.

[22] J. Li, D. Chu, H. Dong, D.R. Baker, R. Jiang, Boosted oxygen evolution reactivity by igniting double exchange interaction in spinel oxides, J. Am. Chem. Soc. 142 (2019) 50-54.

[23] Z. Xue, X. Li, Q. Liu, M. Cai, K. Liu, M. Liu, Z. Ke, X. Liu, G. Li, Interfacial electronic structure modulation of NiTe nanoarrays with NiS nanodots facilitates electrocatalytic oxygen evolution, Adv. Mater. 31 (2019) 1900430.

[24] Y. Yang, M. Luo, W. Zhang, Y. Sun, X. Chen, S. Guo, Metal surface and interface energy electrocatalysis: fundamentals, performance engineering, and opportunities, Chem, 4 (2018) 2054-2083.

[25] Y. Wang, J. Ma, J. Wang, S. Chen, H. Wang, J. Zhang, Interfacial scaffolding preparation of hierarchical PBA-based derivative electrocatalysts for efficient water splitting, Adv. Energy Mater. 9 (2019) 1802939.

[26] D. Guo, Y. Luo, X. Yu, Q. Li, T. Wang, High performance $NiMoO_4$ nanowires supported on carbon cloth as advanced electrodes for symmetric supercapacitors, Nano Energy 8 (2014) 174-182.

[27] G. Yilmaz, C.F. Tan, Y.-F. Lim, G.W. Ho, Pseudomorphic transformation of interpenetrated prussian blue analogs into defective nickel iron selenides for enhanced electrochemical and photo-electrochemical water splitting, Adv. Energy Mater. 9 (2019) 1802983.

[28] Z.Y. Yu, Y. Duan, J.D. Liu, Y. Chen, X.K. Liu, W. Liu, T. Ma, Y. Li, X.S. Zheng, T. Yao, M.R. Gao, J.F. Zhu, B.J. Ye, S.H. Yu, Unconventional CN vacancies suppress iron-leaching in prussian blue analogue pre-catalyst for boosted oxygen evolution catalysis, Nat. Commun. 10 (2019) 2799.

[29] Y.Y. Chen, Y. Zhang, X. Zhang, T. Tang, H. Luo, S. Niu, Z.H. Dai, L.J. Wan, J.S. Hu, Self-templated fabrication of $MoNi_4/MoO_{3-x}$ nanorod arrays with dual active components for highly efficient hydrogen evolution, Adv. Mater. 29 (2017) 1703311.

[30] Y. Ge, P. Dong, S.R. Craig, P.M. Ajayan, M. Ye, J. Shen, Transforming nickel hydroxide into 3D prussian blue analogue array to obtain Ni_2P/Fe_2P for efficient hydrogen evolution reaction, Adv. Energy Mater. 8 (2018) 1800484.

[31] Y. Liu, W. Zhang, S. Li, C. Cui, J. Wu, H. Chen, F. Huo, Designable yolk-shell nanoparticle@MOF petalous heterostructures, Chem. Mater. 26 (2014) 1119-1125.

[32] B.K. Kang, M.H. Woo, J. Lee, Y.H. Song, Z. Wang, Y. Guo, Y. Yamauchi, J.H. Kim, B. Lim, D.H. Yoon, Mesoporous Ni-Fe oxide multi-composite hollow nanocages for efficient electrocatalytic water oxidation reactions, J. Mater. Chem. A 5 (2017) 4320-4324.

[33] S. Lei, Q.-H. Li, Y. Kang, Z.-G. Gu, J. Zhang, Epitaxial growth of oriented prussian blue analogue derived well-aligned $CoFe_2O_4$ thin film for efficient oxygen evolution reaction, Appl. Catal. B: Environ. 245 (2019) 1-9.

[34] D. Ghosh, S. Giri, C.K. Das, Synthesis, characterization and electrochemical performance of graphene decorated with 1D $NiMoO_4 \cdot nH_2O$ nanorods, Nanoscale 5 (2013) 10428-10437.

[35] Y. Duan, Z.Y. Yu, S.J. Hu, X.S. Zheng, C.T. Zhang, H.H. Ding, B.C. Hu, Q.Q. Fu, Z.L. Yu, X. Zheng, J.F. Zhu, M.R. Gao, S.H. Yu, Scaled-up synthesis of amorphous NiFeMo oxides and their rapid surface reconstruction for superior oxygen evolution catalysis, Angew. Chem. Int. Ed. 58 (2019) 15772-15777.

[36] G. Wu, W. Chen, X. Zheng, D. He, Y. Luo, X. Wang, J. Yang, Y. Wu, W. Yan, Z. Zhuang, X. Hong, Y. Li, Hierarchical Fe-doped NiO_x nanotubes assembled from ultrathin nanosheets containing trivalent nickel for oxygen evolution reaction, Nano Energy 38 (2017) 167-174.

[37] J. Zhang, T. Wang, D. Pohl, B. Rellinghaus, R. Dong, S. Liu, X. Zhuang, X. Feng, Interface engineering of MoS_2/Ni_3S_2 heterostructures for highly enhanced electrochemical overall-water-splitting activity, Angew. Chem. Int. Ed. 55 (2016) 6702-6707.

[38] M.A. van Veenendaal, Sawatzky, Nonlocal screening effects in 2p x-ray photoemission spectroscopy core-level line shapes of transition metal compounds, Phys. Rev. Lett. 70

(1993) 2459-2462.

[39] A.P. Grosvenor, M.C. Biesinger, R.S.C. Smart, N.S. McIntyre, New interpretations of XPS spectra of nickel metal and oxides, Surf. Sci. 600 (2006) 1771-1779.

[40] J. Chen, F. Zheng, S. Zhang, A. Fisher, Y. Zhou, Z. Wang, Y. Li, B. Xu, J. Li, S. Sun, Interfacial interaction between FeOOH and Ni−Fe LDH to modulate the local electronic structure for enhanced OER electrocatalysis, ACS Catal. 8 (2018) 11342-11351.

[41] B.C. Moon, W.H. Choi, K.H. Kim, D.G. Park, J.W. Choi, J.K. Kang, Ultrafine metallic nickel domains and reduced molybdenum states improve oxygen evolution reaction of NiFeMo electrocatalysts, Small 15 (2019) 1804764.

[42] D. Klissurski, M. Mancheva, R. Iordanova, G. Tyuliev, B. Kunev, Mechanochemical synthesis of nanocrystalline nickel molybdates, J. Alloys Compd. 422 (2006) 53-57.

[43] C. Xie, Y. Wang, K. Hu, L. Tao, X. Huang, J. Huo, S. Wang, In situ confined synthesis of molybdenum oxide decorated nickel-iron alloy nanosheets from MoO_4^{2-} intercalated layered double hydroxides for the oxygen evolution reaction, J. Mater. Chem. A 5 (2016) 87-91.

[44] J. Sun, N. Guo, Z. Shao, K. Huang, Y. Li, F. He, Q. Wang, A facile strategy to construct amorphous spinel-based electrocatalysts with massive oxygen vacancies using ionic liquid dopant, Adv. Energy Mater. 8 (2018) 1800980.

[45] F. Lei, Y. Sun, K. Liu, S. Gao, L. Liang, B. Pan, Y. Xie, Oxygen vacancies confined in ultrathin indium oxide porous sheets for promoted visible-light water splitting, J. Am. Chem. Soc. 136 (2014) 6826-6829.

[46] H.D. Yang, Y. Liu, S. Luo, Z. Zhao, X. Wang, Y. Luo, Z. Wang, J. Jin, J. Ma, Lateral-size-mediated efficient oxygen evolution reaction: insights into the atomically thin quantum dot structure of $NiFe_2O_4$, ACS Catal. 7 (2017) 5557-5567.

[47] N. Suen, S. Hung, Q. Quan, N. Zhang, Y. Xu, H. M. Chen, Electrocatalysis for the oxygen evolution reaction: recent development and future perspectives, Chem. Soc. Rev. 46 (2017) 337-365.

[48] F. Li, J. Du, X. Li, J. Shen, Y. Wang, Y. Zhu, L. Sun, Integration of FeOOH and zeolitic imidazolate framework-derived nanoporous carbon as an efficient electrocatalyst for water

oxidation, Adv. Energy Mater. 8 (2018) 1702598.

[49] J. Bao, X. Zhang, B. Fan, J. Zhang, M. Zhou, W. Yang, X. Hu, H. Wang, B. Pan, Y. Xi Ultrathin spinel-structured nanosheets rich in oxygen deficiencies for enhanced electrocatalytic water oxidation, Angew. Chem. 127 (2015) 7507-7512.

[50] M. Kim, S. Kim, D. Song, S. Oh, K.J. Chang, E. Cho, Promotion of electrochemical oxygen evolution reaction by chemical coupling of cobalt to molybdenum carbide, Appl. Catal. B: Environ. 227 (2018) 340-348.

[51] M.W. Louie, A.T. Bell, An investigation of thin-film Ni-Fe oxide catalysts for the electrochemical evolution of oxygen, J. Am. Chem. Soc. 135 (2013) 12329-12337.

[52] G. Minrui, S. Wenchao, Z. Zhongbin, F. Qianrong, G. Shuang, J. Jun, Y. Yushan, Efficient water oxidation using nanostructured α-nickel-hydroxide as an electrocatalyst, J. Am. Chem. Soc. 136 (2014) 7077-7084.

[53] V. Vedharathinam, G.G. Botte, Direct evidence of the mechanism for the electro-oxidation of urea on $Ni(OH)_2$ catalyst in alkaline medium, Electrochim. Acta 108 (2013) 660-665.

[54] J. Huang, Y. Li, Y. Zhang, G. Rao, C. Wu, Y. Hu, X. Wang, R. Lu, Y. Li, J. Xiong, Identification of key reversible intermediates in self-reconstructed nickel-based hybrid electrocatalysts for oxygen evolution, Angew. Chem. Int. Ed. 58 (2019) 17458-17464.

[55] Z.W. Gao, J.Y. Liu, X.M. Chen, X.L. Zheng, J. Mao, H. Liu, T. Ma, L. Li, W.C. Wang, X.W. Du, Engineering NiO/NiFe LDH intersection to bypass scaling relationship for oxygen evolution reaction via dynamic tridimensional adsorption of intermediates, Adv. Mater. 31 (2019) 1804769.

Figures

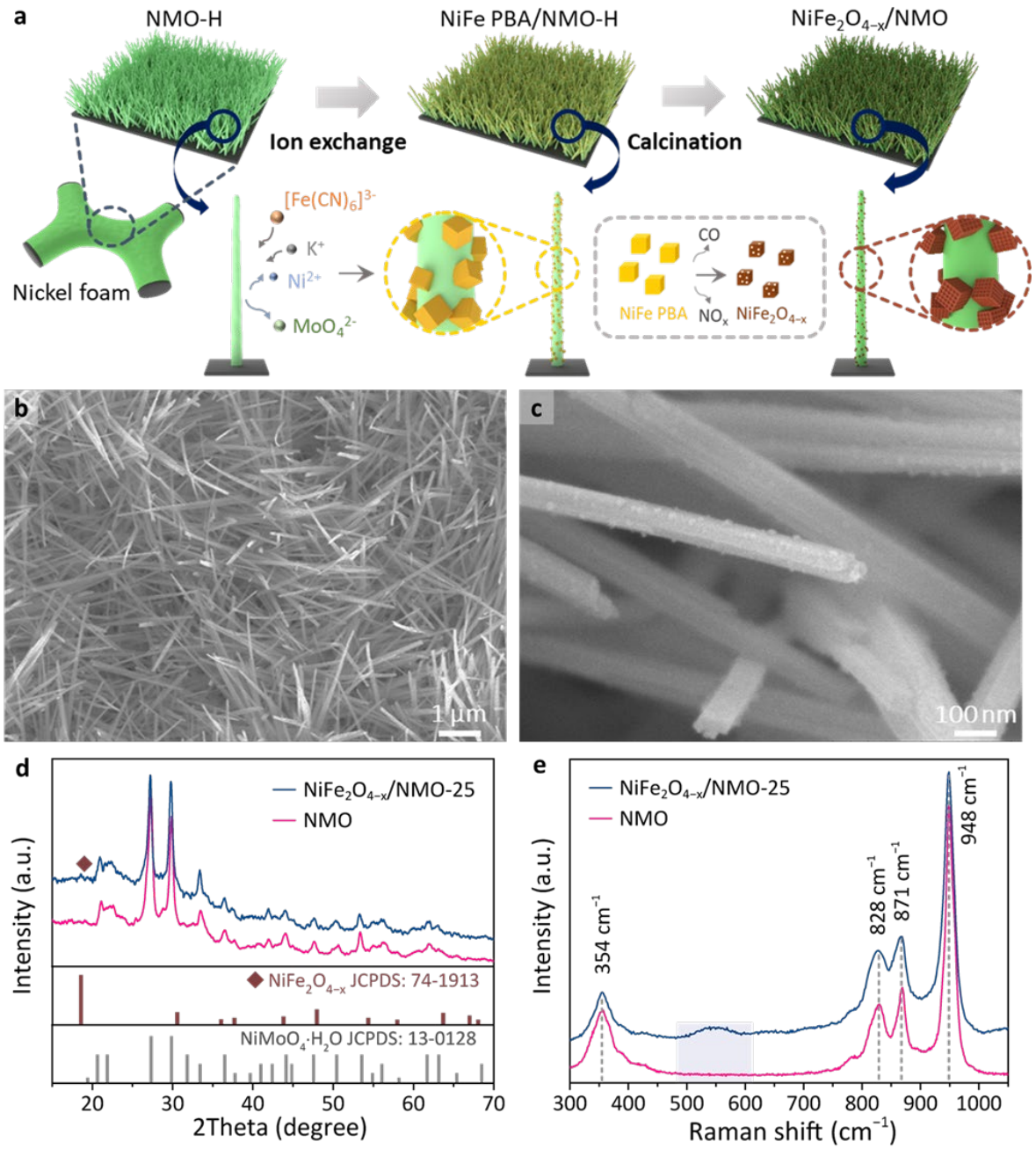

Fig. 1. (a) Schematics illustrating the synthetic procedure of $NiFe_2O_{4-x}$/NMO. (b) Low- and (c) high-magnification SEM images of $NiFe_2O_{4-x}$/NMO-25. (d) XRD patterns and (e) Raman spectra of $NiFe_2O_{4-x}$/NMO-25 and NMO.

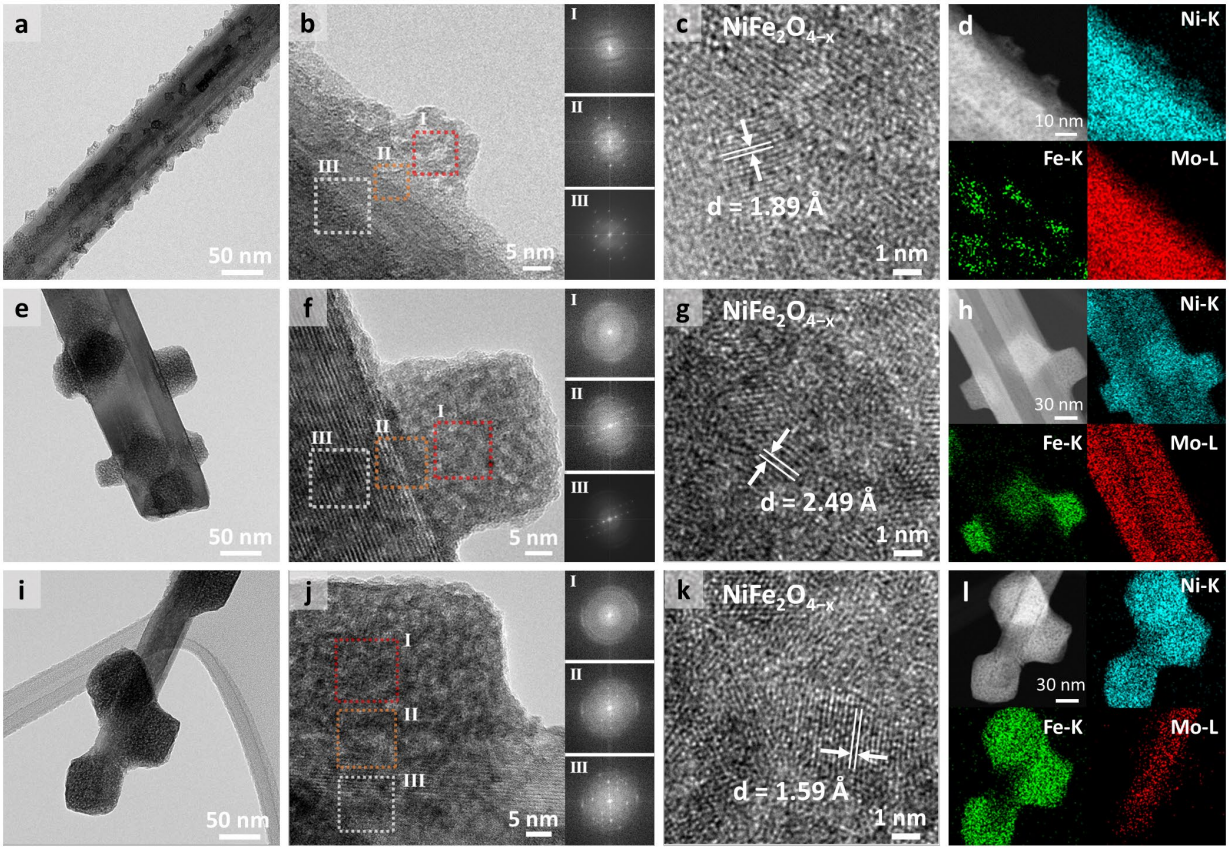

Fig. 2. (a,e,i) TEM images, (b,f,j) HRTEM images and FFT patterns of selected areas (dashed box), (c,g,h) the corresponding HRTEM images of $NiFe_2O_{4-x}$ nanoparticles, and (d,h,l) EDS mapping images for Ni, Fe, and Mo elements of $NiFe_2O_{4-x}$/NMO-25, $NiFe_2O_{4-x}$/NMO-75, and $NiFe_2O_{4-x}$/NMO-100, respectively.

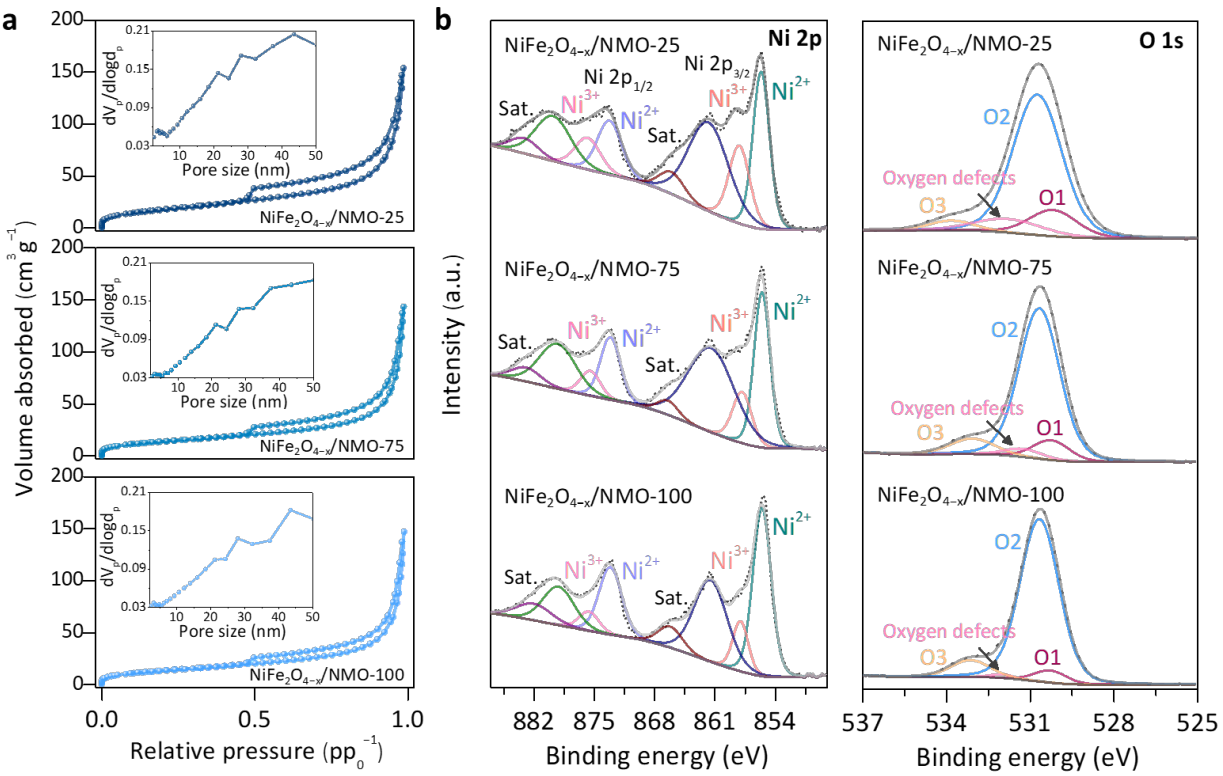

Fig. 3. (a) N_2 adsorption-desorption isotherms and (b) high-resolution Ni 2p and O 1s XPS spectra of $NiFe_2O_{4-x}$/NMO-25, $NiFe_2O_{4-x}$/NMO-75, and $NiFe_2O_{4-x}$/NMO-100. Insets in (a) are the size distribution of mesopores obtained using Barrett-Joyer-Halenda (BJH) method.

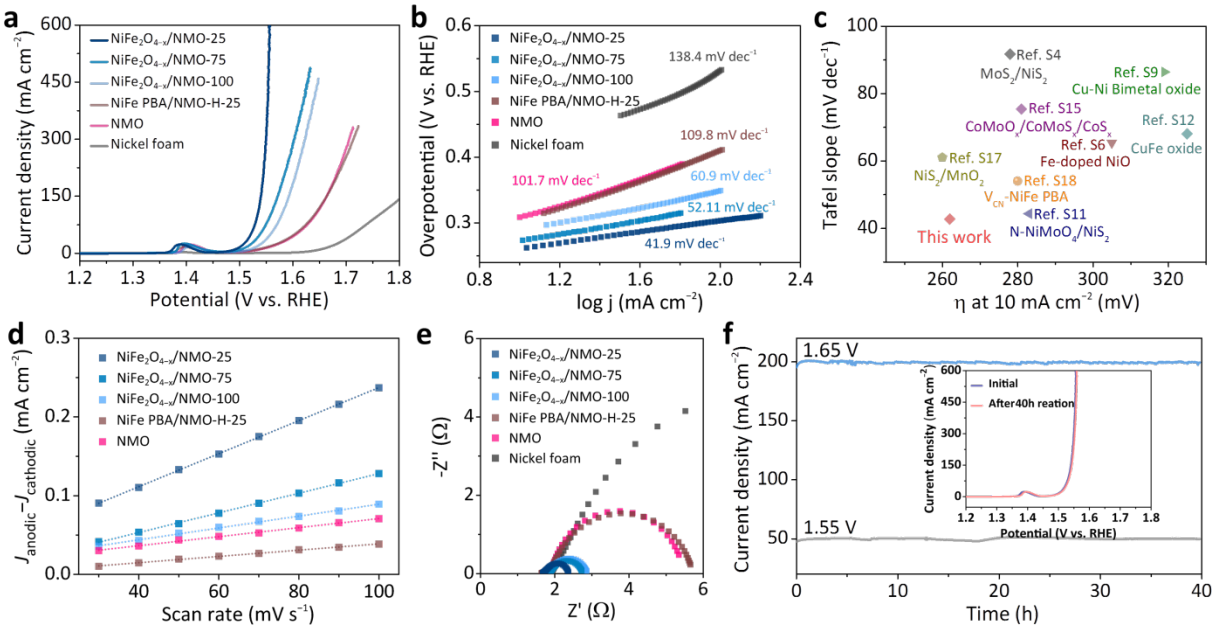

Fig. 4. (a) LSV curves and (b) Tafel plots of as-prepared catalysts. (c) Comparison of overpotentials at 10 mA cm^{-2} and Tafel slopes of $NiFe_2O_{4-x}$/NMO-25 and recently reported analogous catalysts. (d) Capacitive currents plotted as a function of scan rates of as-prepared catalysts. (e) Nyquist plots at 290 mV (*vs*. Hg/HgO) of $NiFe_2O_{4-x}$/NMO-25, $NiFe_2O_{4-x}$/NMO-75, $NiFe_2O_{4-x}$/NMO-100, NiFe PBA/NMO-H-25, NMO, and Ni foam. (f) Chronoamperograms of $NiFe_2O_{4-x}$/NMO-25 at 1.55 and 1.65 V without *i*R-compensation. Inset is the corresponding LSV curves before and after 40 h stability test.

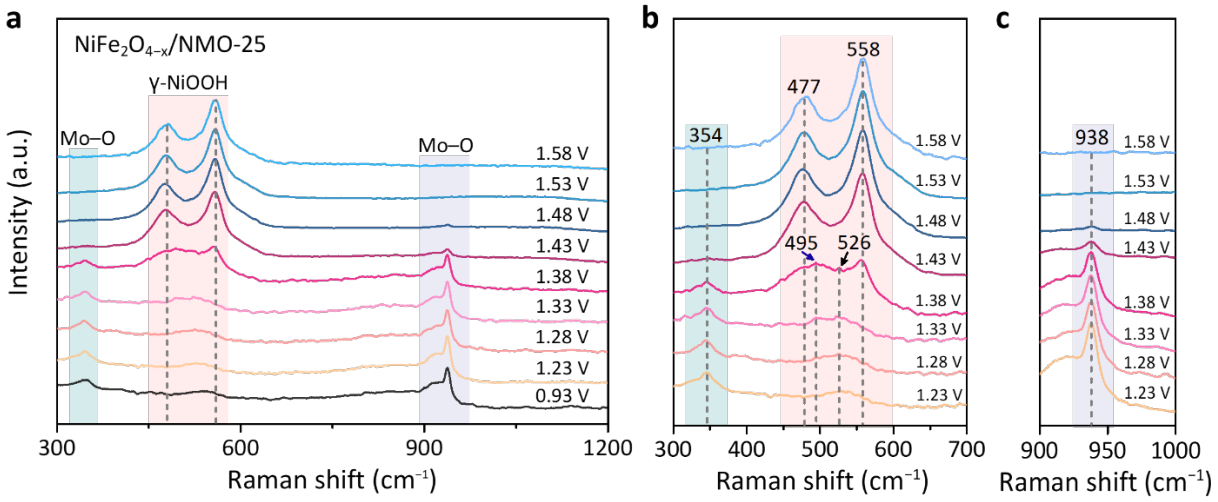

Fig. 5. (a) *In situ* Raman spectra of freshly prepared $NiFe_2O_{4-x}$/NMO-25 in 1 M KOH at various applied potentials for activation. (b, c) Magnification of the corresponding regions in (a) related to the phase transition in the potential range from 1.23 to 1.58 V.

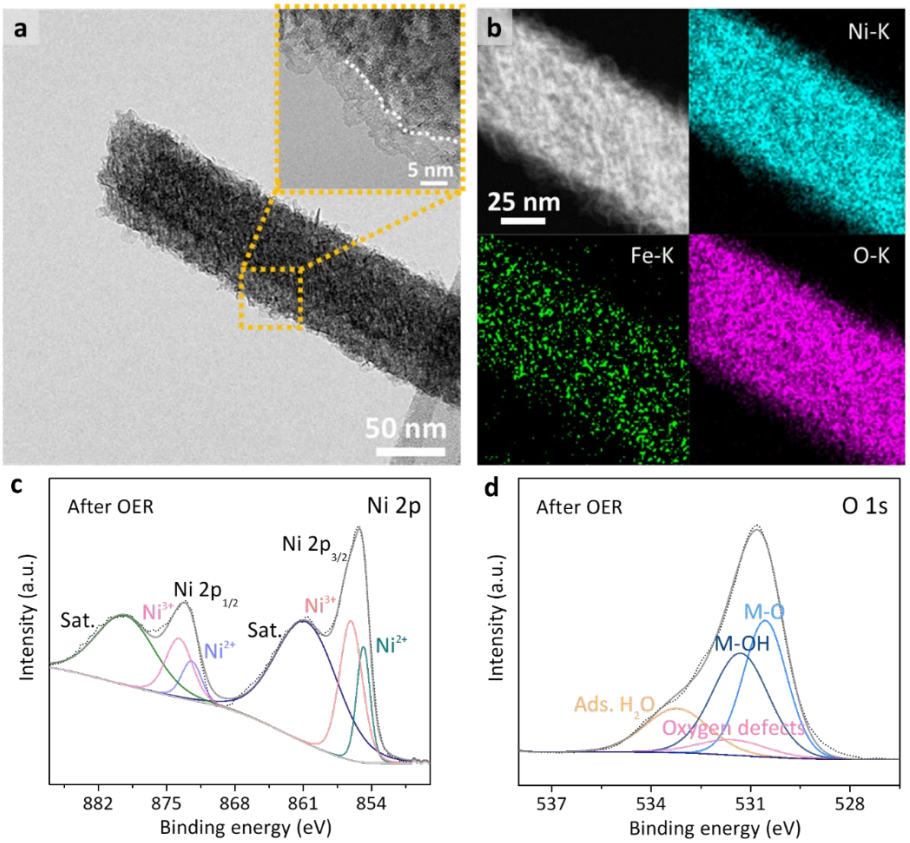

Fig. 6. Structural and XPS analysis of $NiFe_2O_{4-x}$/NMO-25 after OER test. (a) TEM and (b) EDX elemental mappings. Inset in (a) is a HRTEM image of the dashed box. The core level spectra of (c) Ni 2p and (d) O 1s.